

Tachyon Mimetic Inflation as an Instabilities-Free Model

Narges Rashidi* and Kouros Nozari†

*Department of Theoretical Physics, Faculty of Basic Sciences,
University of Mazandaran,
P. O. Box 47416-95447, Babolsar, IRAN*

We consider the mimetic tachyon model in the lagrange multiplier approach. We study both the linear and non-linear perturbations and find the perturbation and non-gaussianity parameters in this setup. By adopting two types of the scale factor as the power-law ($a = a_0 t^n$) and intermediate ($a = a_0 \exp(bt^\beta)$) scale factors, we perform a numerical analysis on the model which is based on Planck2018 TT, TE, EE+lowE+lensing +BAO +BK14 and Planck2018 TTT, EEE, TTE and EET data sets. We show that the mimetic tachyon model with both the power-law and intermediate scale factors, in some ranges of its parameter space is instabilities-free and observationally viable. The power-law mimetic tachyon model with $26.3 < n < 33.0$ and the intermediate mimetic tachyon model with $0.116 < \beta < 0.130$ are consistent with observational data and free of the ghost and gradient instabilities.

PACS: 98.80.Bp, 98.80.Cq, 98.80.Es

Key Words: Tachyon Model, Mimetic Gravity, Cosmological Perturbation, Observational Constraints

I. INTRODUCTION

Although a canonical scalar field, slowly rolling its flat potential, gives a simple model of inflation which solves some problems of the standard model of cosmology, it predicts the scale invariant, adiabatic and almost gaussian dominant modes of the primordial perturbations (precisely, this model predicts small, still non-vanishing primordial non-Gaussianity) [1, 2, 3, 4, 5, 6, 7, 8, 9]. However, some extended models of inflation, predicting the non-Gaussian distributed perturbations, have attracted a lot of attentions [9, 10, 11, 12, 13, 14, 15, 16, 17, 18, 19, 20, 21, 22]. One way to get a model with non-Gaussian distributed perturbations, is to consider the non-canonical scalar field such as DBI or tachyon fields [23, 24, 25, 26, 27, 28, 29, 30, 31, 32, 33, 34]. In this paper, we focus on the tachyon scalar field. It is possible to consider this scalar field, which is associated with D-branes in string theory [27, 28, 29], as responsible for both the early time inflation [30, 35] and late time acceleration [30, 36, 37].

On the other hand, in 2003 Chamseddine and Mukhanov have proposed a new approach to the General Relativity in which a non-dynamical scalar field (ϕ) relates the physical metric ($g_{\mu\nu}$) to an auxiliary metric ($\tilde{g}_{\mu\nu}$) as follows [38]

$$g_{\mu\nu} = -\tilde{g}^{\alpha\beta} \phi_{,\alpha} \phi_{,\beta} \tilde{g}_{\mu\nu}. \quad (1)$$

This proposal, called mimetic gravity, has this important property that respects the conformal symmetry as an internal degree of freedom [38]. Also, the definition (1) ensures that by performing a weyl transformation on the auxiliary metric, the physical metric remains invariant.

In the mimetic gravity, there is the following constraint

$$g^{\mu\nu} \phi_{,\mu} \phi_{,\nu} = -1, \quad (2)$$

obtained from equation (1). The contribution of the matter fields coupled to $g_{\mu\nu}$ in the action of the mimetic gravity, leads to an extra term in the Einstein's field equations corresponding to a^{-3} . This extra term in the field equations, which mimics the matter component, is considered as a source of the dark matter [38]. The mimetic gravity scenario can be studied in another approach by considering the lagrange multipliers in the action of the theory, as proposed in Refs. [39, 40, 41]. In Ref. [42], the authors have studied some models of the mimetic gravity which are ghost-free. Also, considering a potential term for the mimetic field leads to some interesting cosmological results. This case has been discussed in [43]. Several extension of the mimetic gravity have been studied by authors, such as the braneworld mimetic scenario [44], non-minimal coupling in the mimetic model [45, 46], $f(G)$ model of the mimetic gravity [47], Horndeski mimetic gravity [39, 48], unimodular $f(R)$ mimetic gravity [49], $f(R)$ theories in the mimetic model [50, 51, 52] and Galileon mimetic gravity [53]. The (in)stability issue in the mimetic gravity is an important subject that has attracted a lot of attentions. In fact, the authors seek for the mimetic models which are free of the ghost and gradient instabilities [54, 55, 56, 57, 58, 59, 60, 61, 62, 63, 64, 65, 66, 67, 68]. In this regard, the authors of Ref. [69] have shown that by considering the direct coupling between the curvature of the space-time and the higher derivatives of the mimetic field, it is possible to have an instabilities-free mimetic model in some ranges of the parameter space. Also, in Ref. [70] the authors have studied the Higher-derivatives Lagrangian model to show the possibility of evading from instabilities. However, in Ref. [33] it has been shown that, considering a DBI mimetic gravity model is one way to overcome the ghost and gradient instabilities in the mimetic gravity.

* n.rashidi@umz.ac.ir

† knozari@umz.ac.ir

In this paper, we assume the tachyon field to be the mimetic field, study the inflation and perturbations in this model and compare the results with observational data. From planck2018 data, we have some constraints on the perturbation and non-gaussianity parameters by which we can explore the observational viability of the inflation models. In fact, by assuming Λ CDM + r + $\frac{dn_s}{d\ln k}$ model, Planck2018 TT, TE, EE+lowE+lensing+BAO+BK14 data gives the constraint on the scalar spectral index as $n_s = 0.9658 \pm 0.0038$ and the constraint on the tensor-to-scalar ratio as $r < 0.072$, respectively [71, 72]. The constraint on the tensor spectral index, implied by Planck2018 TT, TE, EE+lowE+lensing+BK14+BAO+LIGO and Virgo2016 data is $-0.62 < n_T < 0.53$ [71, 72]. Also, Planck2018 TTT, EEE, TTE and EET data gives the constraint on the equilateral amplitude of the non-gaussianity as $f^{equil} = -26 \pm 47$ [10]. By numerical studying of these parameters in our inflation model and compare the results with released data, it is possible to constraint the model's parameters observationally.

The paper is organized as follows: In section 2, we study the mimetic tachyon model and obtain the main equations of the model. In section 3, we consider both the linear and non-linear perturbations and find perturbation and non-linear parameters in the mimetic tachyon model. In section 4, we reconstruct the model in terms of the e-folds number. The power-law inflation in the mimetic tachyon model is studied in section 5. In this section, we show this model is free of instabilities. We also find the perturbation and non-gaussianity parameters in terms of the model's parameter. We perform a numerical analysis on the model and compare the results with several observational data sets to obtain some constraints on the model's parameter space. In section 6, we study the intermediate inflation in the mimetic tachyon model. In this section also, by performing a numerical analysis, we explore the (in)stability issue and the observational viability of the model. In section 7, we present a summary of the paper.

II. MIMETIC TACHYON MODEL

We consider the following action for the mimetic tachyon model in the lagrange multiplier approach

$$S = \int d^4x \sqrt{-g} \left[\frac{1}{2\kappa^2} R - V(\phi) \sqrt{1 - 2\alpha\dot{\phi}^2} + \lambda(g^{\mu\nu} \partial_\mu \phi \partial_\nu \phi + 1) \right], \quad (3)$$

where, R is the Ricci scalar, $V(\phi)$ presents potential of the tachyon field, α is the constant warp factor. Also, $X = -\frac{1}{2} \partial_\mu \phi \partial^\mu \phi$ and the parameter λ is a lagrange multiplier, entering the mimetic constraint (2) in the action.

Note that, in the Lagrangian formalism generally one is not allowed to impose the constraints on the action

from the beginning. This is an important point in the lagrangian formalism. We should first obtain the main equations of motions and then impose the constraints, as it has been done in paper [33]. In this regard, we show that the mimetic tachyon action (3) leads to nonzero sound speed providing the propagating curvature perturbation. The Einstein's field equations in the mimetic tachyon model are obtained by varying action (3) with respect to the metric

$$G_{\mu\nu} = \kappa^2 \left[-g_{\mu\nu} V(\phi) \sqrt{1 - 2\alpha\dot{\phi}^2} + \frac{\alpha V(\phi) \partial_\mu \phi \partial_\nu \phi}{\sqrt{1 - 2\alpha\dot{\phi}^2}} + g_{\mu\nu} \lambda (g^{\mu\nu} \partial_\mu \phi \partial_\nu \phi + 1) - 2\lambda \partial_\mu \phi \partial_\nu \phi \right]. \quad (4)$$

In the flat FRW background with the metric

$$ds^2 = -dt^2 + a^2(t) \delta_{ij} dx^i dx^j, \quad (5)$$

and from the field equations (4), we obtain the following Friedmann equations

$$3H^2 = \kappa^2 \left[\frac{V}{\sqrt{1 - \alpha\dot{\phi}^2}} - \lambda(1 + \dot{\phi}^2) \right], \quad (6)$$

$$2\dot{H} + 3H^2 = \kappa^2 \left[V \sqrt{1 - \alpha\dot{\phi}^2} + \lambda(\dot{\phi}^2 - 1) \right]. \quad (7)$$

Variation of the action (3) with respect to the tachyon field gives the following equation of motion in the mimetic tachyon model

$$\frac{\alpha \ddot{\phi}}{1 - \alpha\dot{\phi}^2} + 3\alpha H \dot{\phi} - 2\lambda(\ddot{\phi} + 3H\dot{\phi}) + \frac{V'}{V} - \lambda'(1 - \dot{\phi}^2) = 0. \quad (8)$$

To study the inflation and observational viability of the mimetic tachyon model, we should obtain the slow-roll parameters in this model. These parameters are obtained from the following definitions

$$\epsilon \equiv -\frac{\dot{H}}{H^2}, \quad \eta \equiv \frac{1}{H} \frac{d \ln \epsilon}{dt}, \quad s \equiv \frac{1}{H} \frac{d \ln c_s}{dt}, \quad (9)$$

where c_s is the sound speed of the primordial perturbations. This parameter is defined as $c_s^2 = \frac{P_{,X}}{\rho_{,X}}$ where, P is the pressure, ρ is the energy density and the subscript “ X ” demonstrates derivative of the parameter with respect to X . In this regard, the square of the sound speed in the mimetic tachyon model is given by

$$c_s^2 = -\frac{2\kappa^{-2} \dot{H} (1 - \alpha\dot{\phi}^2)^{\frac{3}{2}}}{\left[2(\alpha\dot{\phi}^2 - 1) \lambda \sqrt{-\alpha\dot{\phi}^2 + 1 + V\alpha} \right] \dot{\phi}^2} = \frac{(\alpha\dot{\phi}^2 - 1) \left(2\lambda \sqrt{-\alpha\dot{\phi}^2 + 1 - V\alpha} \right)}{2(\alpha\dot{\phi}^2 - 1) \lambda \sqrt{-\alpha\dot{\phi}^2 + 1 + V\alpha}}. \quad (10)$$

If $0 < c_s^2 \leq c^2$, the model is free of gradient instability [73, 74].

To seek for the observational viability of the mimetic tachyon model, in the following we study the perturbations in this setup and obtain the perturbation and non-gaussian parameters in this setup.

III. PERTURBATIONS IN THE MIMETIC TACHYON MODEL

In this section, we study the perturbations in our mimetic tachyon setup in both linear and non-linear level which help us to explore the model and its viability, in details.

A. Linear perturbation

We start with the perturbed ADM line element given by

$$ds^2 = -(1 + 2\mathcal{R})dt^2 + 2a(t)\Upsilon_i dt dx^i + a^2(t)[(1 - 2\Psi)\delta_{ij} + 2\Theta_{ij}] dx^i dx^j, \quad (11)$$

where $\Upsilon^i = \delta^{ij}\partial_j\Upsilon + v^i$. The vector v^i satisfies the condition $v^i_{;i} = 0$ and also \mathcal{R} and Υ are 3-scalars [75]. In this perturbed metric, we have denoted the spatial curvature perturbation by Ψ and the spatial symmetric and traceless shear 3-tensor by Θ_{ij} . Now, we consider just the scalar part of the the perturbations at the linear level as

$$ds^2 = -(1 + 2\mathcal{R})dt^2 + 2a(t)\Upsilon_{,i} dt dx^i + a^2(t)(1 - 2\Psi)\delta_{ij} dx^i dx^j, \quad (12)$$

written within the uniform-field gauge ($\delta\phi = 0$). We can use the perturbed metric (12) and expand the action (3) up to the second order in the perturbations as

$$S_2 = \int dt d^3x a^3 \mathcal{W} \left[\dot{\Psi}^2 - \frac{c_s^2}{a^2} (\partial\Psi)^2 \right], \quad (13)$$

which is named the quadratic action and where the parameter c_s^2 is given by equation (10). Also, the parameter \mathcal{W} is defined as

$$\begin{aligned} \mathcal{W} &= \frac{\left[2 \left(\alpha \dot{\phi}^2 - 1 \right) \lambda \sqrt{-\alpha \dot{\phi}^2 + 1 + V \alpha} \right] \dot{\phi}^2}{2 H^2 \left(1 - \alpha \dot{\phi}^2 \right)^{\frac{3}{2}}} \\ &= \frac{-\frac{3}{4} \dot{\phi}^2 \left(\left(2 \alpha \dot{\phi}^2 - 2 \right) \lambda \sqrt{-\alpha \dot{\phi}^2 + 1 + V \alpha} \right)}{\left(\left(-\dot{\phi}^2 - 1 \right) \lambda \sqrt{-\alpha \dot{\phi}^2 + 1 + V} \right) \kappa^2 \left(\frac{1}{2} \alpha \dot{\phi}^2 - \frac{1}{2} \right)}. \end{aligned} \quad (14)$$

One of the perturbation parameters which is constrained by the observational data, is the scalar spectral index.

To obtain this parameter in the mimetic tachyon model, we use the following two-point correlation function

$$\langle 0 | \Psi(0, \mathbf{k}_1) \Psi(0, \mathbf{k}_2) | 0 \rangle = (2\pi)^3 \delta^{(3)}(\mathbf{k}_1 + \mathbf{k}_2) \frac{2\pi^2}{k^3} \mathcal{A}_s, \quad (15)$$

with the power spectrum defined as

$$\mathcal{A}_s = \frac{H^2}{8\pi^2 \mathcal{W} c_s^3}. \quad (16)$$

Now, it is possible to find the scale dependence of the perturbation as

$$n_s - 1 = \left. \frac{d \ln \mathcal{A}_s}{d \ln k} \right|_{c_s k = aH}. \quad (17)$$

The scalar spectral index, n_s , in terms of the slow-roll parameters is obtained as

$$n_s = 1 - 2\epsilon - \eta - s. \quad (18)$$

By writing the 3-tensor Θ_{ij} of the tensor part of the perturbed metric (11), in terms of the two polarization tensors ($\vartheta_{ij}^{(+,\times)}$) as $\Theta_{ij} = \Theta_+ \vartheta_{ij}^+ + \Theta_\times \vartheta_{ij}^\times$, one can obtain the following expression for the second order action of the tensor mode

$$S_T = \int dt d^3x \frac{a^3}{4\kappa^2} \left[\dot{\Theta}_+^2 - \frac{1}{a^2} (\partial\Theta_+)^2 + \dot{\Theta}_\times^2 - \frac{1}{a^2} (\partial\Theta_\times)^2 \right]. \quad (19)$$

Following the method used in the scalar part, leads to the amplitude of the tensor perturbations as

$$\mathcal{A}_T = \frac{2\kappa^2 H^2}{\pi^2}. \quad (20)$$

By using equations (27)-(29), we find the tensor spectral index in this setup as

$$n_T = \frac{d \ln \mathcal{A}_T}{d \ln k} = -2\epsilon. \quad (21)$$

Another important perturbation parameter is the tensor-to-scalar ratio which is defined as

$$r = \frac{\mathcal{A}_T}{\mathcal{A}_s} = 16c_s\epsilon. \quad (22)$$

By performing a numerical analysis on n_s , n_T and r and comparing the results with the observational data, we can find some constraints on the model's parameter space. After obtaining the parameters describing the linear perturbations, in the next subsection, we study the non-linear perturbations to seek for the non-gaussian feature of the primordial perturbations and more constraints on the model's parameters.

B. Non-linear Perturbations

In studying the primordial perturbations, the linear level of the perturbations gives us no information about the non-gaussian feature. Therefore, we should go to the non-linear level of the perturbations and use the three-point correlation function. In this regard, by expanding the action (3) up to the third order in the small perturbations, and introducing the new parameter Υ satisfying

$$\Upsilon = \frac{\Psi}{H} + \kappa^2 a^2 \mathcal{Z}, \quad (23)$$

and

$$\partial^2 \mathcal{Z} = \mathcal{W} \dot{\Psi}, \quad (24)$$

we find the cubic action, up to the leading order in the slow-roll parameters of the model, as follows

$$S_3 = \int dt d^3x \left\{ \left[\frac{3a^3}{\kappa^2 c_s^2} \left(1 - \frac{1}{c_s^2} \right) \epsilon \right] \Psi \dot{\Psi}^2 + \left[\frac{a}{\kappa^2} \left(\frac{1}{c_s^2} - 1 \right) \epsilon \right] \Psi (\partial \Psi)^2 + \left[\frac{a^3}{\kappa^2} \left(\frac{1}{c_s^2 H} \right) \left(\frac{1}{c_s^2} - 1 \right) \epsilon \right] \dot{\Psi}^3 - \left[a^3 \frac{2}{c_s^2} \epsilon \dot{\Psi} (\partial_i \Psi) (\partial_i \mathcal{Z}) \right] \right\}. \quad (25)$$

In the interaction picture, we have the following expression for the three-point correlation function for the the spatial curvature perturbation [9, 76]

$$\begin{aligned} & \langle \Psi(\mathbf{k}_1) \Psi(\mathbf{k}_2) \Psi(\mathbf{k}_3) \rangle \\ &= (2\pi)^3 \delta^3(\mathbf{k}_1 + \mathbf{k}_2 + \mathbf{k}_3) \mathcal{B}_\Psi(\mathbf{k}_1, \mathbf{k}_2, \mathbf{k}_3), \end{aligned} \quad (26)$$

where

$$\mathcal{B}_\Psi(\mathbf{k}_1, \mathbf{k}_2, \mathbf{k}_3) = \frac{(2\pi)^4 \mathcal{A}_s^2}{\prod_{i=1}^3 k_i^3} \mathcal{E}_\Psi(\mathbf{k}_1, \mathbf{k}_2, \mathbf{k}_3), \quad (27)$$

and the power spectrum \mathcal{A}_s^2 is defined by equation (16). The parameter \mathcal{E}_Ψ is given by

$$\begin{aligned} \mathcal{E}_\Psi &= \left(1 - \frac{1}{c_s^2} \right) \left[\frac{3}{4} \left(\frac{2 \sum_{i>j} k_i^2 k_j^2}{k_1 + k_2 + k_3} - \frac{\sum_{i \neq j} k_i^2 k_j^3}{(k_1 + k_2 + k_3)^2} \right) \right. \\ &\quad \left. - \frac{1}{4} \left(\frac{2 \sum_{i>j} k_i^2 k_j^2}{k_1 + k_2 + k_3} - \frac{\sum_{i \neq j} k_i^2 k_j^3}{(k_1 + k_2 + k_3)^2} + \frac{1}{2} \sum_i k_i^3 \right) \right. \\ &\quad \left. - \frac{3}{2} \left(\frac{(k_1 k_2 k_3)^2}{(k_1 + k_2 + k_3)^3} \right) \right] \equiv \left(1 - \frac{1}{c_s^2} \right) \Upsilon, \end{aligned} \quad (28)$$

where, the expression inside the square bracket is replaced by Υ . By using the parameter \mathcal{E}_Ψ , the following so-called ‘‘non-linearity parameter’’, measuring the amplitude of the non-gaussianity, is defined

$$f = \frac{10}{3} \frac{\mathcal{E}_\Psi}{\sum_{i=1}^3 k_i^3}. \quad (29)$$

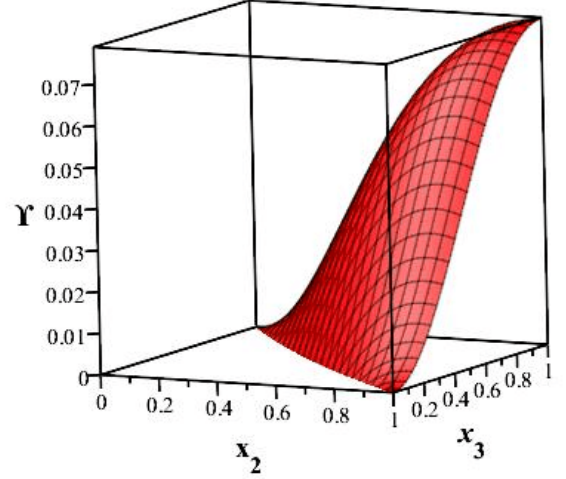


FIG. 1. 3D plot of the function Υ versus $x_2 \equiv \frac{k_2}{k_1}$ and $x_3 \equiv \frac{k_3}{k_1}$. The figure shows that there is a peak for Υ at $k_1 = k_2 = k_3$.

The non-linearity parameter depends on the values of the momenta k_1 , k_2 and k_3 . Also, the different values of the momenta lead to different shapes of the primordial non-gaussianity. For every shape, there is a special configuration of three momenta, leading to a maximal signal of the amplitude of the non-gaussianity. In our model, there is a maximal signal in the equilateral configuration which has been shown in figure 1. Note that, to plot this figure, we have introduced the parameters $x_2 \equiv \frac{k_2}{k_1}$ and $x_3 \equiv \frac{k_3}{k_1}$ and we see that there is a peak at $k_1 = k_2 = k_3$ (also, in Refs. [77, 78, 79] it has been shown that in the k-inflation and higher order derivative models the signal becomes maximal at the equilateral configuration). In this regard, in the following, we focus on the equilateral configuration in which we have $k_1 = k_2 = k_3$ [77]. In this limit, we have

$$\mathcal{E}_\Psi^{equil} = \frac{17}{72} k^3 \left(1 - \frac{1}{c_s^2} \right), \quad (30)$$

leading to

$$f^{equil} = \frac{85}{324} \left(1 - \frac{1}{c_s^2} \right). \quad (31)$$

By using this non-linear parameter obtained in the equilateral configuration, we can study the non-gaussian feature of the perturbations in our mimetic tachyon setup numerically.

Note that, to obtain the constraint on f^{equil} , we follow the Planck papers on the non-gaussianity [10, 80, 81]. As has been said in the mentioned papers, it is possible to

use the definition of the amplitude of the non-gaussianity, sound speed and the scalar spectral index in every model to find some constraints on the model's parameters from the observational constraint on f^{equil} . In this way, one can explore the viability of the models. Following the Planck papers, we use the observational constraints on f^{equil} to find the constraints on c_s^2 and therefore model's parameters. Also, we use the constraints on $r - n_s$ to find the constraints on the model's parameters. In this regard, we can present the prediction of our model for non-gaussianity. In this regard, we show that it is possible to find some ranges of the model's parameters which give observationally viable inflation and primordial perturbation. To this end, we should find the potential and the lagrange multiplier in our model which we do in the next sections.

IV. RECONSTRUCTION THE MODEL IN TERMS OF THE E-FOLDS NUMBER

One can write the slow-roll parameters, in terms of the e-folds number defined as

$$N = \int H dt. \quad (32)$$

To this end, we should first find the potential and lagrange multiplier in our model. By using equation (7), and implying the constraint equation (2), we find the potential in the mimetic tachyon model as

$$V = \frac{2H(N)H'(N) + 3H^2(N)}{\sqrt{1 - \alpha\kappa^2}}, \quad (33)$$

where we have used a prime to show a derivative of the parameter with respect to the e-folds number. The lagrange multiplier also is obtained from equations (6) and (33) as follows

$$\lambda = -\frac{3H^2(N)\alpha + 2H(N)H'(N)}{2(-1 + \alpha)\kappa^2}. \quad (34)$$

After obtaining the potential and lagrange multiplier, we find the following expression for the sound speed of the mimetic tachyon model

$$c_s^2 = -\frac{2H'(N)(-1 + \alpha)^2}{(4\alpha - 2)H'(N) + 3H(N)\alpha^2}. \quad (35)$$

Also, the parameter \mathcal{W} is obtained as

$$\mathcal{W} = \frac{H(N)(4\alpha - 2)H'(N) + 3H^2(N)\alpha^2}{2(-1 + \alpha)^2\kappa^2H^2(N)}. \quad (36)$$

To find the slow-roll parameters, following [82, 83], we introduce a new scalar field φ , identified by the number of e-folds N . Also, this new parameter parameterizes the scalar field ϕ as $\phi = \phi(\varphi)$. In this regard, we can write $\dot{\phi}$ as $\dot{\phi} = \frac{d\phi}{d\varphi} \frac{d\varphi}{dt} = \frac{d\phi}{d\varphi} H$, which with constraint

equation (2) gives $\frac{d\phi}{d\varphi} = \frac{1}{H}$. In this way, we have also $\frac{dV}{d\phi} = \frac{dV}{d\varphi} \frac{d\varphi}{d\phi} = H \frac{dV}{dN}$. Now, the slow-roll parameters in the mimetic tachyon model and in terms of the e-folds number are given by

$$\epsilon = \frac{-H'(N)}{2H(N)}, \quad (37)$$

$$\eta = -\frac{H(N)H''(N) + (H'(N))^2}{H(N)H'(N)}, \quad (38)$$

and

$$s = \frac{3\alpha^2 (H(N)H''(N) - (H'(N))^2)}{(8\alpha - 4)(H'(N))^2 + 6H(N)\alpha^2H'(N)}. \quad (39)$$

By using the equations obtained in this section, we can express the perturbation and non-gaussianity parameters in terms of the Hubble parameters and therefore e-folds number. In the following, by adopting some suitable scale factors, we study the mimetic tachyon model numerically.

V. POWER-LAW INFLATION IN THE MIMETIC TACHYON MODEL

To study the power-law inflation in the mimetic tachyon model, we use the following scale factor

$$a = a_0 t^n. \quad (40)$$

By this scale factor, the Hubble parameter is obtained as follows

$$H(N) = n e^{-\frac{N}{n}}. \quad (41)$$

Now, from equations (37)-(41) we find the slow-roll parameters in the power-law mimetic tachyon model as

$$\epsilon = \frac{1}{2n}, \quad \eta = \frac{1}{n}, \quad s = 0. \quad (42)$$

Also, the sound speed is obtained as

$$c_s^2 = \frac{2(-1 + \alpha)^2}{3\alpha^2 n - 4\alpha + 2}, \quad (43)$$

and the parameter \mathcal{W} is given by

$$\mathcal{W} = \frac{3\alpha^2 n - 4\alpha + 2}{2n(-1 + \alpha)^2\kappa^2}. \quad (44)$$

By using these equations we can find the ranges of the parameters α and n leading to gradient and ghost instabilities-free mimetic tachyon model, corresponding to the constraints $0 < c_s^2 \leq 1$ and $\mathcal{W} > 0$. The results are shown in figure 2. As figure shows, the mimetic tachyon model in most ranges of its parameter space is free of instabilities, making it an interesting mimetic gravity model.

We can also study the perturbation parameters numerically to seek for the observational viability of the

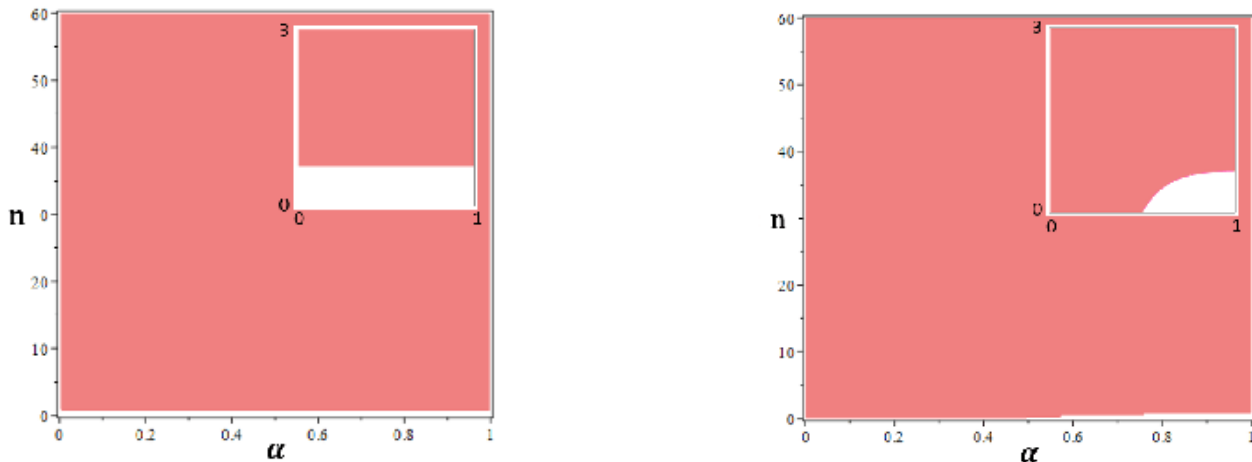


FIG. 2. The coral regions show the ranges of the model's parameters in the power-law mimetic tachyon model which lead to $0 < c_s^2 \leq 1$ (left panel) and $W > 0$ (right panel).

mimetic tachyon model. This gives us more constraints on the model's parameters. By using equations (18) and (42), we can find the scalar spectral index in terms of the model's parameters and study it numerically. The left-upper panel of figure 3 shows the ranges of the parameters α and n which lead to $n_s = 0.9658 \pm 0.0038$, obtained from Planck2018 TT, TE, EE+lowE+lensing +BAO +BK14 data. The right upper panel of this figure shows that the ranges of the model's parameters leading to $r < 0.072$, obtained from same data set. The lower panel of figure 3 demonstrates the range of the parameters α and n which leads to $-0.62 < n_T < 0.53$, obtained from Planck2018 TT, TE, EE+lowE+lensing+BK14+BAO+LIGO and Virgo2016 data. We have also studied the behavior of $r - n_s$ and $r - n_T$ in the background of several data sets at 68% and 95% CL. The results are shown in figure 4 and 5. The constraints obtained from this numerical analysis are summarized in table I.

As mentioned before, the non-gaussian feature of the primordial perturbations is important issue in studying the inflation models. Here, we study the equilateral configuration of the non-gaussianity in comparison with observational data. To numerical study of the equilateral non-gaussianity, we use equation (31), where the sound speed is given by equation (43). By using the combined temperature and polarization data analysis at 68% CL, planck2018 gives the constraint on the equilateral non-gaussianity as $f^{equil} = -26 \pm 47$. From this constraint, we have found the ranges of the model's parameter space leading to the observationally viable values of the non-gaussianity in the equilateral configuration. The result is shown in figure 6. This figure shows in some ranges of the parameter space, we have observationally viable values of the equilateral non-gaussianity. Also, from Planck2018 TTT, EEE, TTE and EET data at 68% CL, the constrain on the sound speed is as $c_s^2 \geq 0.0035$ (this is ob-

tained from the constraint $f^{equil} = -26 \pm 47$ released by Planck2018). Table II, shows the viable ranges of parameter n for some sample values of α , corresponding to this observationally viable range of the square of the sound speed in the power-law mimetic tachyon model. Figure 7 shows the behavior of the equilateral configuration of the non-gaussianity versus the sound speed in the background of the Planck2018 TTT, EEE, TTE and EET data at 68%, 95% and 99.7% CL. This figure shows that the equilateral non-gaussianity versus the sound speed in this model is consistent with observational data. However, note that, every possible value of the sound speed is not observationally viable. In fact, according to the equation (22), the sound speed is related to the tensor-to-scalar ratio. The observationally viable values of r , set some constraints on the sound speed of the primordial perturbation. Figure 8 shows the behavior of the square of the sound speed versus the tensor-to-scalar ratio in the power-law mimetic tachyon model. To plot this figure, we have considered the Planck2018 TT, TE, EE+lowE+lensing +BAO +BK14 data, used in figure 4. From this data analysis, we have found that for $r > 0.44$, the sound speed reach unity and therefore there would be no non-gaussianity in the model. To obtain some constraints on the sound speed and the nonlinear parameter, we use the constraints on n , obtained in studying $r - n_s$ behavior in comparison with observational data. The results are shown in table III. According to our analysis and considering both Planck2018 TT, TE, EE+lowE+lensing +BAO +BK14 and Planck2018 TTT, EEE, TTE and EET data sets at 68% CL, the power-law mimetic tachyon model is observationally viable if $26.3 < n < 33.0$ and $0.310 < \alpha < 0.398$. In these ranges, the model is instabilities-free and also the perturbation and non-gaussianity parameters are observationally viable.

Note that, the Planck observational data has implied

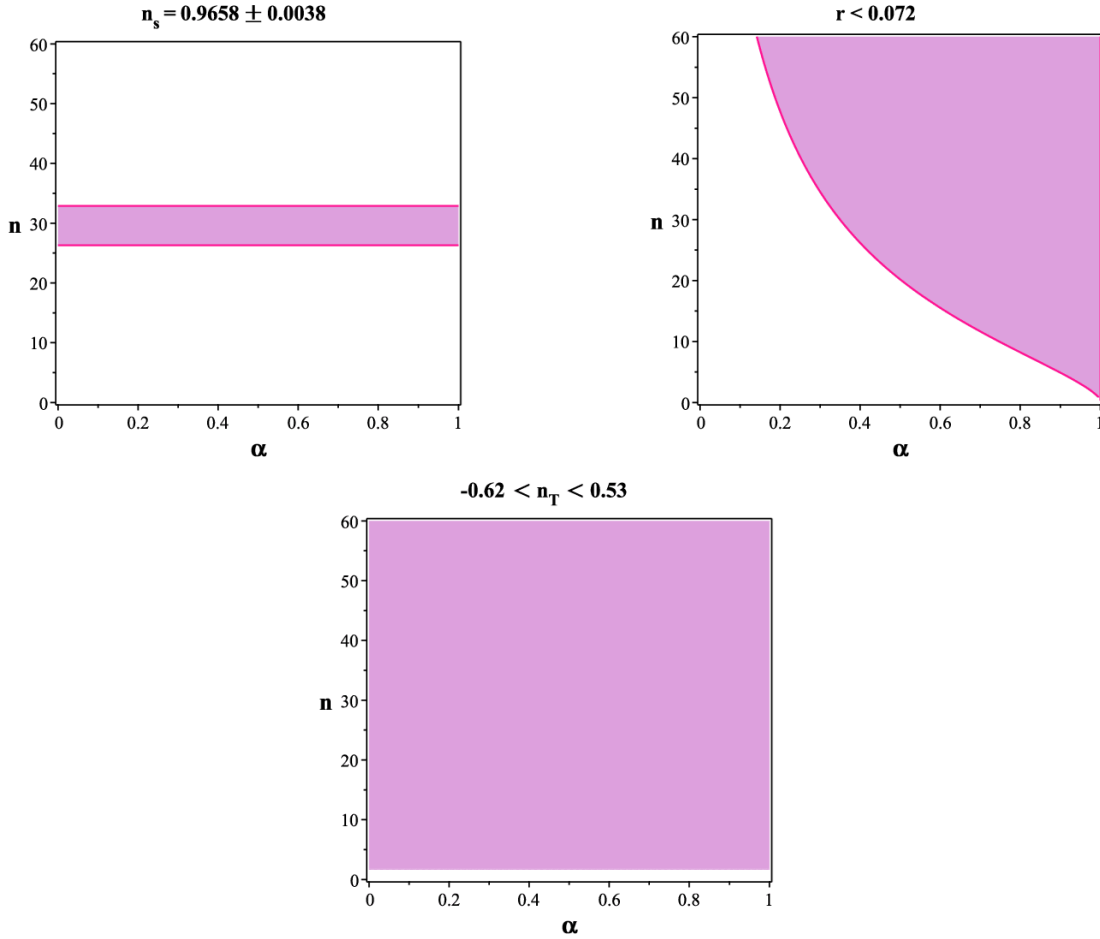


FIG. 3. The plum regions in the upper panels demonstrate the ranges of the model's parameters in the power-law mimetic tachyon model leading to the observationally viable values of the scalar spectral index (left one) and tensor-to-scalar ratio (right one), which are obtained from Planck2018 TT, TE, EE+lowE+lensing +BAO +BK14 data. The plum regions in the lower panel shows the range of the model's parameters leading to the observationally viable values of the tensor spectral index, which is obtained from Planck2018 TT, TE, EE +lowE+lensing+BK14+BAO+LIGO and Virgo2016 data.

TABLE I. The ranges of the model's parameters in which the tensor-to-scalar ratio, the scalar spectral index and the tensor spectral index of the power-law mimetic tachyon model are consistent with different data sets.

	Planck2018 TT,TE,EE+lowE +lensing+BK14+BAO	Planck2018 TT,TE,EE+lowE +lensing+BK14+BAO	Planck2018 TT,TE,EE+lowE lensing+BK14+BAO +LIGO&Virgo2016	Planck2018 TT,TE,EE+lowE lensing+BK14+BAO LIGO&Virgo2016
α	68% CL	95% CL	68% CL	95% CL
0.3	not consistent	$32.4 < n < 38.5$	$38.1 < n < 230.2$	$30.5 < n$
0.5	$27.9 < n < 36.4$	$25.3 < n < 42.1$	$22.6 < n < 130.3$	$18.4 < n$
0.8	$26.1 < n < 36.2$	$24.0 < n < 41.1$	$9.60 < n < 52.4$	$7.90 < n$

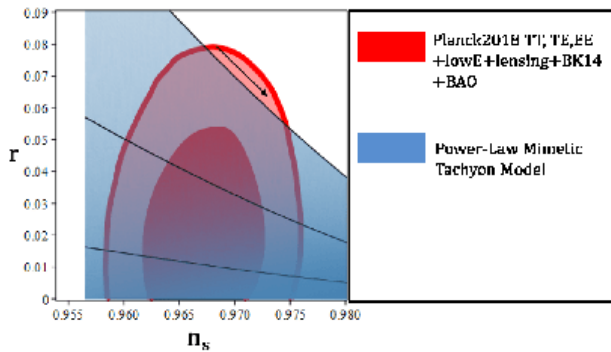


FIG. 4. Tensor-to-scalar ratio versus the scalar spectral index of the power-law mimetic tachyon model. The black lines have been drawn to show the behavior of $r - n_s$. The parameter n increases in the direction of the arrow.

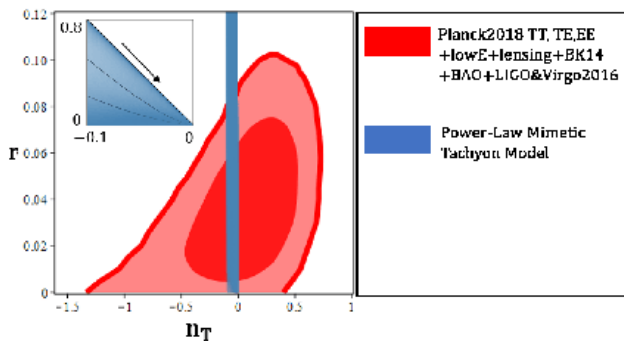


FIG. 5. Tensor-to-scalar ratio versus the tensor spectral index of the power-law mimetic tachyon model. We have also zoomed the $r - n_T$ plot out to see its evolution clearly. The parameter n increases in the direction of the arrow.

an upper bound on the tensor-to-scalar ratio. However, there are also some constraints on the scalar spectral index. When we study $r - n_s$ behavior in our model, we see that as r becomes smaller, the scalar spectral index becomes larger. In this regard, there would be both upper and lower limits on the tensor-to-scalar ratio in our model which beyond those limits the scalar spectral in-

TABLE II. The ranges of the model's parameters in which the equilateral configuration of the non-gaussianity in the power-law mimetic tachyon model is consistent with the Planck2018 TTT, EEE, TTE and EET data at 68% CL.

$\alpha = 0.3$	$\alpha = 0.5$	$\alpha = 0.8$
$n < 1010$	$n < 186$	$n < 12.2$

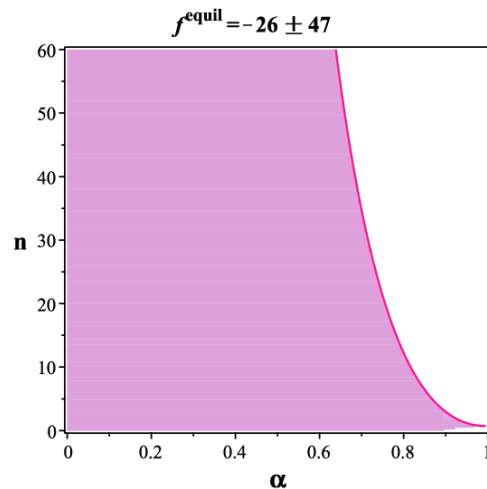


FIG. 6. The plum region shows the ranges of the model's parameters in the power-law mimetic tachyon model leading to the observationally viable values of the equilateral amplitude of the non-gaussianity, which is obtained from Planck2018 TTT, EEE, TTE and EET data.

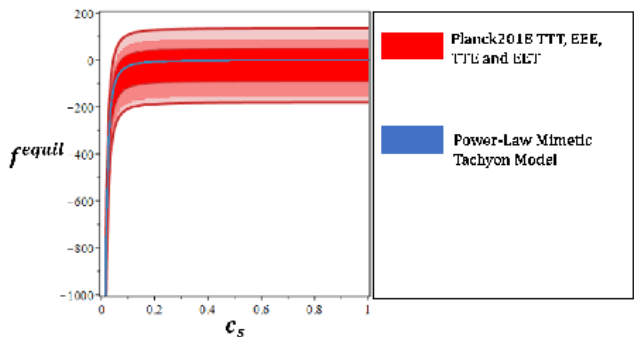


FIG. 7. The amplitude of the non-gaussianity in the equilateral configuration versus the sound speed in the power-law mimetic tachyon model.

dex is not observationally viable anymore. The existence of these limits on r leads to the upper and lower limits on c_s^2 . Also, we didn't fix ϵ . This parameter is defined by equation (42) which is in terms of the model's parameters. To obtain the constraints, we have used these equations.

VI. INTERMEDIATE INFLATION IN THE MIMETIC TACHYON MODEL

In this section, we study the intermediate inflation in the mimetic tachyon model. The intermediate inflation is described by the following scale factor [84, 85, 86]

$$a = a_0 \exp(bt^\beta), \quad (45)$$

TABLE III. The observationally viable ranges of the several parameters in the power-law mimetic tachyon, obtained from Planck2018 TT, TE, EE+lowE+lensing+BAO+BK14 data at 68% CL.

α	r	c_s^2	f^{equil}
0.5	$0.029 < r < 0.044$	$0.0173 < c_s^2 < 0.0238$	$-14.0 < f^{equil} < -10.7$
0.8	$0.007 < r < 0.012$	$0.117 \times 10^{-2} < c_s^2 < 0.163 \times 10^{-2}$	$-223 < f^{equil} < -160$

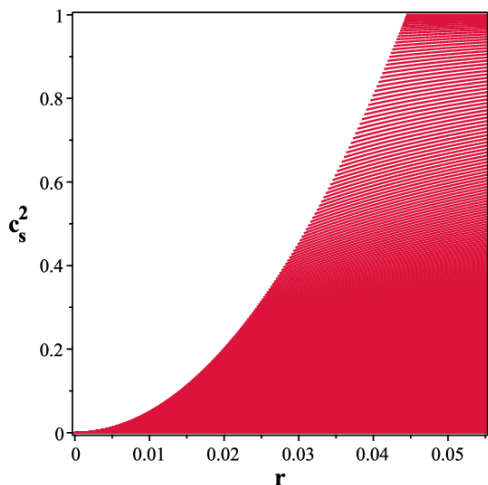


FIG. 8. The square of the sound speed versus the tensor-to-scalar ratio in the power-law mimetic tachyon model.

where, $0 < \beta < 1$ and b is a constant. The above scale factor of the intermediate inflation demonstrates that its evolution is faster than the power law inflation ($a = t^p$) but slower than the standard de Sitter inflation ($a = \exp(Ht)$). By using the scale factor (45), we get the following Hubble parameter

$$H(N) = N \left(\frac{N}{b} \right)^{-\frac{1}{\beta}} \beta. \quad (46)$$

The slow-roll parameters in the intermediate mimetic tachyon model, obtained from equations (37)-(39) and (46), take the following forms

$$\epsilon = \frac{\beta - 1}{2N\beta}, \quad \eta = \frac{2 - \beta}{N\beta},$$

$$s = \frac{-3\beta\alpha^2}{6\beta\alpha^2N + (8\beta - 8)\alpha - 4\beta + 4}. \quad (47)$$

Also, c_s^2 and \mathcal{W} are obtained as

$$c_s^2 = \frac{2(1 - \beta)(-1 + \alpha)^2}{3\beta\alpha^2N + (4\beta - 4)\alpha - 2\beta + 2}, \quad (48)$$

$$\mathcal{W} = \frac{3\beta\alpha^2N + (4\beta - 4)\alpha - 2\beta + 2}{2\beta N(-1 + \alpha)^2\kappa^2}. \quad (49)$$

The ranges of α and n leading to gradient and ghost instabilities-free intermediate mimetic tachyon model are shown in figure 9. This ranges are corresponding to the constraints $0 < c_s^2 \leq 1$ and $\mathcal{W} > 0$. From this figure, we find out that the intermediate mimetic tachyon model too, in some ranges of its parameter space, is free of gradient and ghost instabilities.

As previous section, we study the perturbation parameters to check the observational viability of the intermediate mimetic tachyon model. By substituting equation (47) in equations (18), (21) and (22), we obtain the perturbation parameters in terms of the model's parameter. Now, we can study the model numerically and compare the results with several observational data sets. The left-upper panel of figure 10 shows the ranges of the parameters α and β leading to $n_s = 0.9658 \pm 0.0038$. This constraint is obtained from Planck2018 TT, TE, EE+lowE+lensing +BAO +BK14 data. From the same data set, we have $r < 0.072$, leading to the range shown in the right-upper panel of figure 10. The lower panel of figure 10 demonstrates the range of the parameters α and n which leads to $-0.62 < n_T < 0.53$, obtained from Planck2018 TT, TE, EE+lowE+lensing+BK14+BAO+LIGO and Virgo2016 data. As before, to obtain some constraints on the model's parameters, we have studied the behavior of $r - n_s$ and $r - n_T$ in the background of several data sets at 68% and 95% CL. The results are shown in figure 11 and 12. Table IV shows the constraints obtained from this numerical analysis. Note that, in the numerical analysis of this section we adopt $N = 60$ and $b = 10$.

Now, we study non-gaussian feature to find more information about the viability of the intermediate mimetic tachyon model. Here also, we consider the equilateral configuration of the primordial non-gaussianity with $k_1 = k_2 = k_3$. By using equation (31), where the sound speed is given by equation (48), we can perform a numerical analysis on the equilateral non-gaussianity. From the constraint $f^{equil} = -26 \pm 47$, obtained from the Planck2018 combined temperature and polarization data

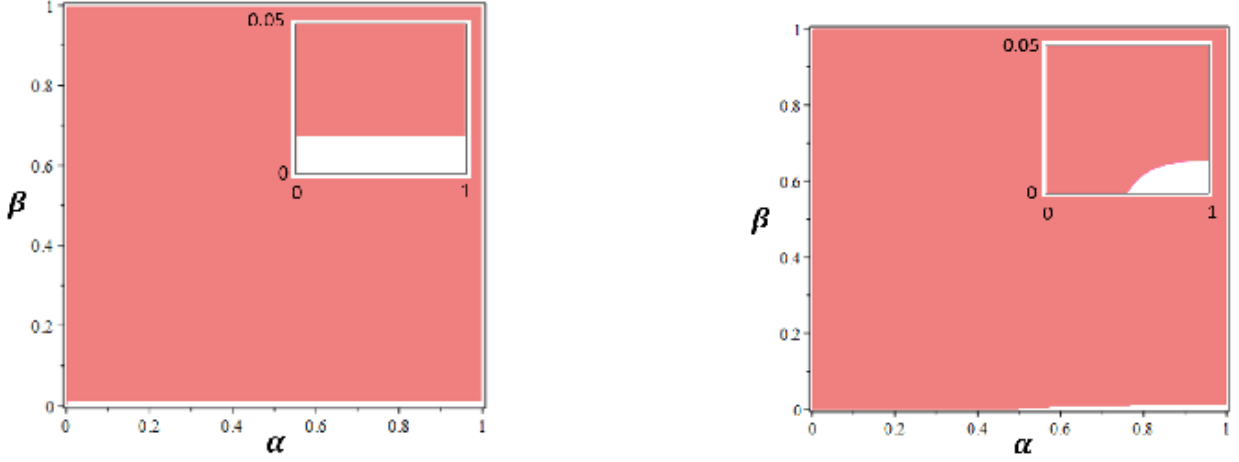


FIG. 9. The coral regions show the ranges of the model's parameters in the intermediate mimetic tachyon model which lead to $0 < c_s^2 \leq 1$ (left panel) and $\mathcal{W} > 0$ (right panel).

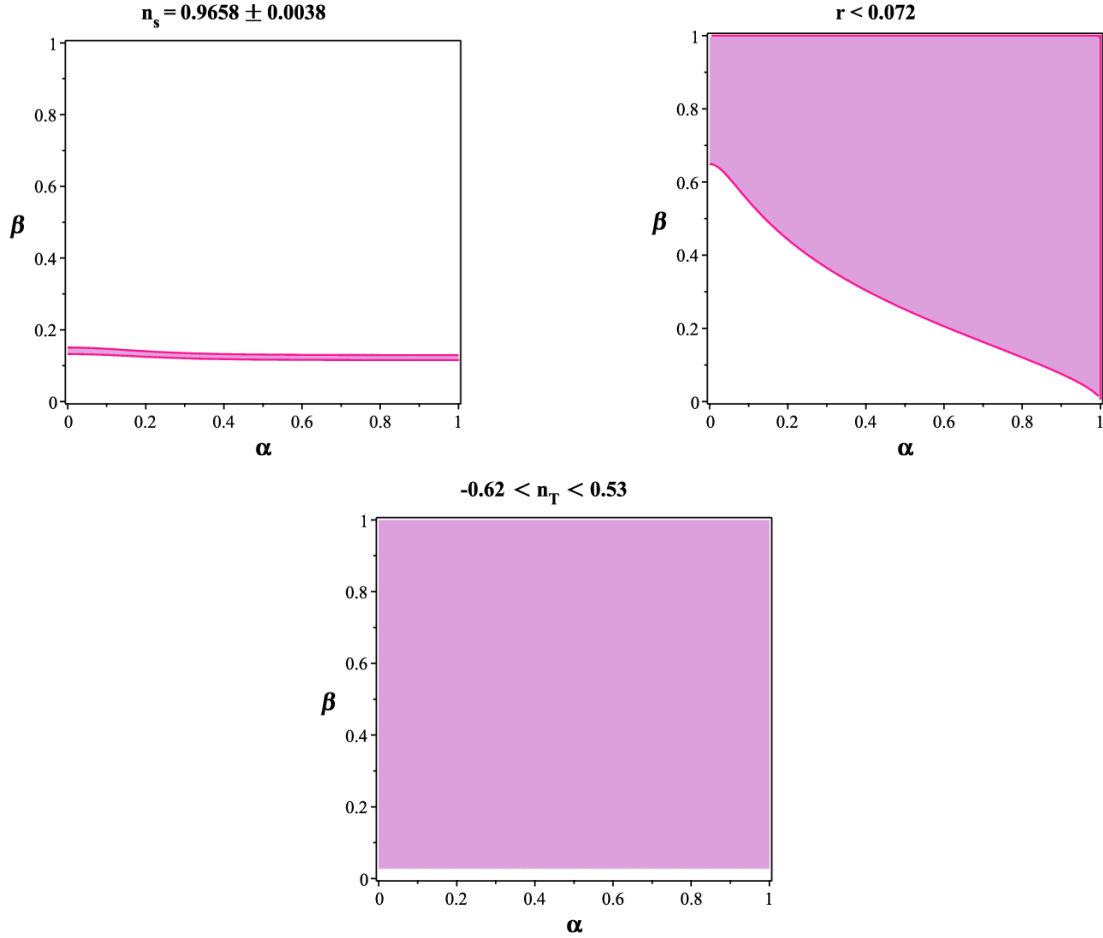


FIG. 10. The plum regions in the upper panels demonstrate the ranges of the model's parameters in the intermediate mimetic tachyon model leading to the observationally viable values of the scalar spectral index (left one) and tensor-to-scalar ratio (right one), which are obtained from Planck2018 TT, TE, EE+lowE+lensing +BAO +BK14 data. The plum regions in the lower panel shows the range of the model's parameters leading to the observationally viable values of the tensor spectral index, which is obtained from Planck2018 TT, TE, EE +lowE+lensing+BK14+BAO+LIGO and Virgo2016 data.

TABLE IV. The ranges of the model's parameters in which the tensor-to-scalar ratio, the scalar spectral index and the tensor spectral index in the intermediate mimetic tachyon model are consistent with different data sets.

	Planck2018 TT,TE,EE+lowE +lensing+BK14+BAO	Planck2018 TT,TE,EE+lowE +lensing+BK14+BAO	Planck2018 TT,TE,EE+lowE lensing+BK14+BAO +LIGO&Virgo2016	Planck2018 TT,TE,EE+lowE lensing+BK14+BAO LIGO&Virgo2016
α	68% CL	95% CL	68% CL	95% CL
0.8	not consistent	$0.119 < \beta < 0.141$	$0.138 < \beta < 0.455$	$0.116 < \beta < 1$
0.85	$0.122 < \beta < 0.133$	$0.114 < \beta < 0.143$	$0.115 < \beta < 0.411$	$0.097 < \beta < 1$
0.9	$0.117 < \beta < 0.136$	$0.111 < \beta < 0.144$	$0.091 < \beta < 0.332$	$0.076 < \beta < 1$

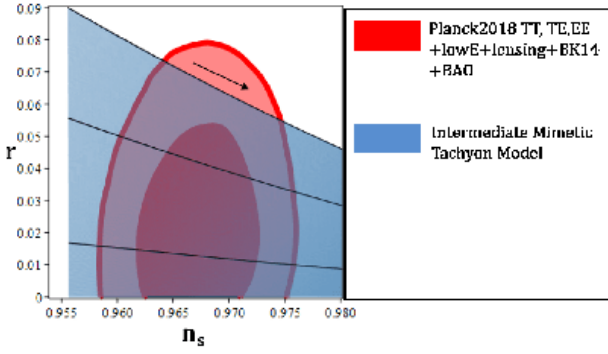


FIG. 11. Tensor-to-scalar ratio versus the scalar spectral index in the intermediate mimetic tachyon model. The black lines have been drawn to show the behavior of $r - n_s$. The parameter n increases in the direction of the arrow.

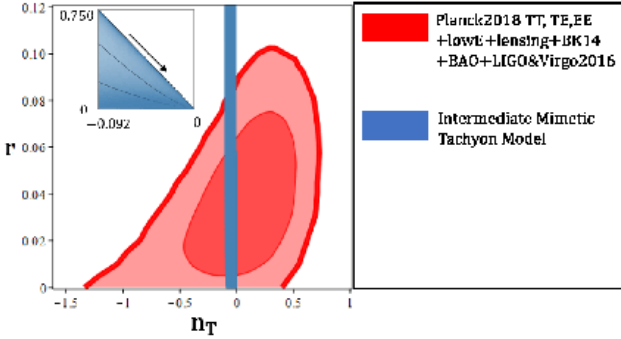


FIG. 12. Tensor-to-scalar ratio versus the tensor spectral index in the intermediate mimetic tachyon model. We have also zoomed the $r - n_T$ plot out to see its evolution clearly. The parameter n increases in the direction of the arrow.

analysis at 68% CL, we have found the observationally viable range of α and β , as shown in figure 13. Also, as mentioned before, from the constraint on f^{equil} , we have $c_s^2 \geq 0.0035$ which gives the viable ranges of pa-

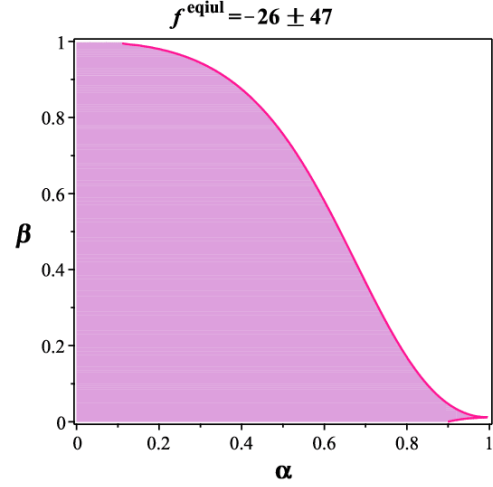


FIG. 13. The plum region shows the ranges of the model's parameters in the intermediate mimetic tachyon model leading to the observationally viable values of the equilateral configuration of the non-gaussianity, which is obtained from Planck2018 TTT, EEE, TTE and EET data.

TABLE V. The ranges of the model's parameters in which the equilateral configuration of the non-gaussianity in the intermediate mimetic tachyon model is consistent with the Planck2018 TTT, EEE, TTE and EET data at 68% CL.

$\alpha = 0.8$	$\alpha = 0.85$	$\alpha = 0.9$
$0.0103 < \beta < 0.169$	$0.0106 < \beta < 0.096$	$0.0108 < \beta < 0.046$

rameter β in the intermediate mimetic tachyon model. These ranges, for some sample values of α , are summarized in table V. The behavior of the equilateral configuration of the non-gaussianity versus the sound speed in the background of the Planck2018 TTT, EEE, TTE and EET data at 68%, 95% and 99.7% CL is shown in figure 14. In the intermediate case also, it is necessary to

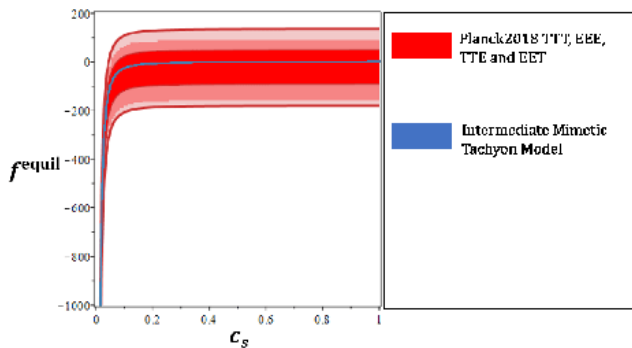


FIG. 14. The amplitude of the non-gaussianity in the equilateral configuration versus the sound speed in the intermediate mimetic tachyon model.

find the observationally viable values of the sound speed. In this regard, we use the equation (22) and the observationally viable values of r , to set some constraints on the sound speed. The result is shown in figure 15. To plot this figure also, we have considered the Planck2018 TT, TE, EE+lowE+lensing +BAO +BK14 data, used in figure 11. From this numerical analysis, we have found that the constraint on the sound speed in the intermediate mimetic tachyon model is as $c_s^2 < 0.668$ at 68% CL. From the constraints on β in table IV, we have obtained some constraints on the sound speed and the nonlinear parameter, summarized in table VI. According to our analysis and based on both Planck2018 TT, TE, EE+lowE+lensing +BAO +BK14 and Planck2018 TTT, EEE, TTE and EET data sets at 68%, the intermediate mimetic tachyon model is observationally viable if $0.778 < \alpha < 0.810$ and $0.116 < \beta < 0.130$. In these ranges, the model is free of ghost and gradient instabilities and also the perturbation and non-gaussianity parameters are observationally viable.

VII. SUMMARY AND CONCLUSION

In this paper we have studied the tachyon model in the context of the mimetic gravity and lagrange multiplier approach. We have assumed that the scalar field in the tachyon model is a mimetic field. In this regard, we have obtained the Einstein's field equations, corresponding Friedmann equations and the equation of motion. After that, we have studied both the linear and non-linear perturbations in the mimetic tachyon model and found perturbations and non-gaussianity parameters in terms of the potential of the mimetic tachyon field and the lagrange multiplier. Then, we have constructed the model in terms of the Hubble parameter and e-folds number. This reconstruction has prepared us to study the mimetic tachyon model for two types of the inflation: power-law and intermediate inflation.

By adopting the power-law scale factor $a = a_0 t^n$,

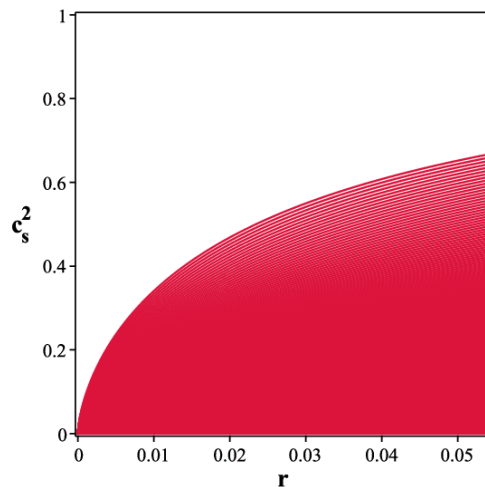


FIG. 15. The square of the sound speed versus the tensor-to-scalar ratio in the intermediate mimetic tachyon model.

we have obtained the slow-roll parameters, sound speed and \mathcal{W} in terms of n and α (the constant warp factor). By performing a numerical analysis on these parameters, we have shown that the power-law mimetic tachyon model in some ranges of its parameter space is free of gradient and ghost instabilities (corresponding to $0 < c_s^2 \leq 1$ and \mathcal{W} , respectively). We have also studied the perturbation parameters n_s , r and n_T numerically and compared the results with Planck2018 TT, TE, EE+lowE+lensing +BAO +BK14 and Planck2018 TTT, TE, EE +lowE+lensing+BK14+BAO+LIGO and Virgo2016 data sets. In this regard, we have obtained some constraints on the parameters n and α , shown in several figures and tables. We have also explored the non-gaussian feature of the primordial perturbation numerically, to find more information about the observational viability of the model. To this end, we have considered the equilateral configuration of the non-gaussianity with $k_1 = k_2 = k_3$. By using the observational constraint on the equilateral amplitude of the non-gaussianity, we have obtained the ranges of the parameters n and α leading to the viable values of f^{equil} . Then, we have used the relation between the equilateral non-gaussianity and the sound speed and also the relation between the sound speed and the tensor-to-scalar ratio, to find some more constraint on the model's parameter space. Our data analysis, based on both Planck2018 TT, TE, EE+lowE+lensing +BAO +BK14 and Planck2018 TTT, EEE, TTE and EET data sets at 68% CL, shows that the power-law mimetic tachyon model is observationally viable and free of instabilities, if $26.3 < n < 33.0$ and $0.310 < \alpha < 0.398$.

We have also checked the mimetic tachyon model with the intermediate scale factor $a = a_0 \exp(bt^\beta)$. By this scale factor, we have obtained ϵ , η , s , c_s^2 and \mathcal{W} in terms of the intermediate parameters and warp factor. We have analyzed the parameters c_s^2 and \mathcal{W}

TABLE VI. The observationally viable ranges of the several parameters in the intermediate mimetic tachyon, obtained from Planck2018 TT, TE, EE+lowE+lensing +BAO +BK14 data at 68% CL.

α	r	c_s^2	f^{equil}
0.85	$0.042 < r < 0.049$	$0.242 \times 10^{-2} < c_s^2 < 0.269 \times 10^{-2}$	$-107 < f^{equil} < -96.9$
0.9	$0.025 < r < 0.033$	$0.936 \times 10^{-3} < c_s^2 < 0.112 \times 10^{-2}$	$-279 < f^{equil} < -232$

numerically and have shown that the intermediate mimetic tachyon model in some ranges of the model's parameter space is instabilities-free. By performing a numerical analysis on the perturbation parameters and comparing the results with Planck2018 TT, TE, EE+lowE+lensing +BAO +BK14 and Planck2018 TT, TE, EE +lowE+lensing+BK14+BAO+LIGO and Virgo2016 data sets, we have found some constraints on the model's parameters, which are shown in several figures and tables. A numerical analysis on the non-gaussian feature of the primordial perturbation in the intermediate mimetic tachyon model has shown that it is possible to have the observationally viable values

of the equilateral configuration of the amplitude of the non-gaussianity in this model. In summary, using both Planck2018 TT, TE, EE+lowE+lensing +BAO +BK14 and Planck2018 TTT, EEE, TTE and EET data sets at 68% CL, shows that the intermediate mimetic tachyon model is observationally viable and free of ghost instabilities, if $0.778 < \alpha < 0.810$ and $0.116 < \beta < 0.130$.

Acknowledgement

We thank the referee for the very insightful comments that have improved the quality of the paper considerably.

-
- [1] A. Guth, Phys. Rev. D **23**, 347 (1981).
[2] A. D. Linde, Physics Letters B **108**, 389 (1982).
[3] A. Albrecht & P. Steinhard, Phys. Rev. D **48**, 1220 (1982).
[4] A. D. Linde, Particle Physics and Inflationary Cosmology (Harwood Academic Publishers, Chur, Switzerland) (1990).
[5] A. R. Liddle & D. Lyth, Cosmological Inflation and Large-Scale Structure, (Cambridge University Press) (2000).
[6] J. E. Lidsey, A. R. Liddle, E. W. Kolb, E. J. Copeland, T. Barreiro & M. Abney, Rev. Mod. Phys. **69**, 373 (1997).
[7] A. Riotto, [arXiv:hep-ph/0210162] (2002).
[8] D. H. Lyth & A. R. Liddle, The Primordial Density Perturbation (Cambridge University Press) (2009).
[9] J. M. Maldacena, JHEP **0305**, 013 (2003).
[10] Y. Akrami, F. Arroja, M. Ashdown, J. Aumont, C. Baccigalupi, et al., [arXiv:1905.05697] (2019).
[11] N. Bartolo, E. Komatsu, S. Matarrese & A. Riotto, Physics Reports **402**, 103 (2004).
[12] X. Chen, Adv. Astron **2010**, 638979 (2010).
[13] S. Nojiri & S. D. Odintsov, Phys. Rev. D **505**, 59 (2011).
[14] A. De Felice & S. Tsujikawa, JCAP **1104**, 029 (2011).
[15] A. De Felice & S. Tsujikawa, Phys. Rev. D **84**, 083504 (2011).
[16] K. Nozari & N. Rashidi, Adv. High Energy Phys **2016**, Article ID 1252689 (2015).
[17] K. Nozari, R. Aghabararian, N. Rashidi Astrophysics and Space Science **358** (2), 24 (2015).
[18] K. Nozari & N. Rashidi, Phys. Rev. D **93**, 124022 (2016).
[19] S. Nojiri, S. D. Odintsov & V. K. Oikonomou, Physics Reports , **692**, 1 (2017).
[20] K. Nozari & N. Rashidi, Phys. Rev. D **95**, 123518 (2017).
[21] K. Nozari & N. Rashidi, The Astrophysical Journal **863**, 133 (2018).
[22] N. Rashidi & K. Nozari, The Astrophysical Journal **890**, 55 (2020).
[23] E. Silverstein & D. Tong, Phys. Rev. D **70**, 103505 (2004).
[24] X. Chen, M. -X. Huang, S. Kachru & G. Shiu, JCAP **0701**, 002 (2007).
[25] M. Alishahiha, E. Silverstein & D. Tong, Phys. Rev. D **70**, 123505 (2004).
[26] X. Chen, JHEP **0508**, 045 (2005).
[27] A. Sen, JHEP **10**, 008 (1999).
[28] A. Sen, JHEP **07**, 065 (2002).
[29] A. Sen, Modern Physics Letters A **17**, 1797 (2002).
[30] K. Nozari & N. Rashidi, Phys. Rev. D **88**, 023519 (2013).
[31] K. Nozari & N. Rashidi, Phys. Rev. D **88**, 084040 (2013).
[32] N. Rashidi & K. Nozari, International Journal of Modern Physics D **27**, 1850076 (2018).
[33] K. Nozari & N. Rashidi, The Astrophysical Journal **882**, 78 (2019).
[34] N. Rashidi, K. Nozari, Ø. Grøn, Journal of Cosmology and Astroparticle Physics **05**, 044 (2018).
[35] M. Sami, P. Chingangbam & T. Qureshi, Phys. Rev. D

- 66**, 043530 (2002).
- [36] E. J. Copeland, M. R. Garousi, M. Sami & S. Tsujikawa, *Phys. Rev. D* **71**, 043003 (2005).
- [37] T. Padmanabhan, *Phys. Rev. D* **66**, 021301 (2002).
- [38] A. Chamseddine & V. Mukhanov, *JHEP* **1311**, 135 (2013).
- [39] F. Arroja, N. Bartolo, P. Karmakar & S. Matarrese, *JCAP* **1509**, 051 (2015).
- [40] A. Golovnev, *Physics Letters B* **728**, 39-40 (2014).
- [41] K. Hammer & A. Vikman, [arXiv:1512.09118] (2015).
- [42] A. O. Barvinsky, *JCAP* **01**, 014 (2014).
- [43] A. Chamseddine, V. Mukhanov & A. Vikman, *JCAP* **1406**, 017 (2014).
- [44] N. Sadeghnezhad & K. Nozari, *Physics Letters B* **769**, 134 (2017).
- [45] R. Myrzakulov, L. Sebastiani & S. Vagnozzi, *The European Physical Journal C* **75**, 444 (2015).
- [46] N. Hosseinkhan & K. Nozari, *The European Physical Journal Plus* **133**, 50 (2018).
- [47] A. V. Astashenok, S. D. Odintsov & V. K. Oikonomou, *Classical and Quantum Gravity* **32**, 185007 (2015).
- [48] G. Cognola, R. Myrzakulov, L. Sebastiani, S. Vagnozzi & S. Zerbini, *Classical and Quantum Gravity* **33**, 225014 (2016).
- [49] S. D. Odintsov & V. K. Oikonomou, *Astrophys. Space Sci* **361**, 174 (2016).
- [50] S. Nojiri & S. D. Odintsov, *Modern Physics Letters A* **29**, 1450211 (2014).
- [51] A. V. Astashenok & S. D. Odintsov, *Phys. Rev. D* **94**, 063008 (2016).
- [52] S. Nojiri, S. D. Odintsov & V. K. Oikonomou, *Phys. Rev. D* **94**, 104050 (2016).
- [53] Z. Haghani, T. Harko, H. R. Sepangi & S. Shahidi, [arXiv:1404.7689] (2014).
- [54] A. Ijjas, J. Ripley & P. J. Steinhardt, *Physics Letters B* **760**, 132 (2016).
- [55] F. Capela & S. Ramazanov, *JCAP* **1504**, 051 (2015).
- [56] L. Mirzaghali & A. Vikman, *JCAP* **1506**, 028 (2015).
- [57] O. Malaeb, *Phys. Rev. D* **91**, 103526 (2015).
- [58] S. Ramazanov, *JCAP* **1512**, 007 (2015).
- [59] D. Langlois & K. Noui, *JCAP* **1607**, 016 (2016).
- [60] S. Ramazanov, F. Arroja, M. Celoria, S. Matarrese & L. Pilo, *JHEP* **06**, 020 (2016).
- [61] F. Arroja, N. Bartolo, P. Karmakar & S. Matarrese, *JCAP* **1604**, 042 (2016).
- [62] J. B. Achour, D. Langlois, & K. Noui, *Phys. Rev. D* **93**, 124005 (2016).
- [63] S. Hirano, S. Nishi & T. Kobayashi, *JCAP* **1707**, 009 (2017).
- [64] Y. Cai & Y. -S. Piao, *Phys. Rev. D* **96**, 124028 (2017).
- [65] K. Takahashi & T. Kobayashi, *JCAP* **11**, 038 (2017).
- [66] D. Yoshida, J. Quintin, M. Yamaguchi & R. H. Brandenberger, *Phys. Rev. D* **96**, 043502 (2017).
- [67] A. Ganz, P. Karmakar, S. Matarrese & D. Sorokin, *Phys. Rev. D* **99**, 064009 (2019).
- [68] D. Langlois, M. Mancarella, K. Noui & F. Vernizzi, doi: <https://doi.org/10.1088/1475-7516/2019/02/036>, (2018).
- [69] Y. Zheng, L. Shen, Y. Mou & M. Li, *JCAP* **08**, 040 (2017).
- [70] A. Ganz and K. Noui, [arXiv:2007.01063] (2020).
- [71] N. Aghanim, Y. Akrami, M. Ashdown, J. Aumont, C. Baccigalupi, et al., [arXiv:1807.06209] (2018).
- [72] Y. Akrami, F. Arroja, M. Ashdown, J. Aumont, C. Baccigalupi, et al., [arXiv:1807.06211] (2018).
- [73] E. Ellis, R. Maartens & M. A. H. MacCallum, *General Relativity and Gravitation* **39**, 1651 (2007).
- [74] I. Quiros, T. Gonzalez, U. Nucamendi & R. Garcia-Salcedo, *Classical and Quantum Gravity* **35**, 075005 (2018).
- [75] V. F. Mukhanov, H. A. Feldman & R. H. Brandenberger, *Physics Reports* **215**, 203 (1992).
- [76] C. Cheung, P. Creminelli, A. L. Fitzpatrick, J. Kaplan & L. Senatore, *JHEP* **03**, 014 (2008).
- [77] D. Babich, P. Creminelli & M. Zaldarriaga, *JCAP* **0408** 09 (2004).
- [78] A. De Felice & S. Tsujikawa, *JCAP* **03**, 030 (2011).
- [79] D. Baumann, [arXiv:0907.5424] (2012).
- [80] P. A. R. Ade, et al., DOI: <https://doi.org/10.1051/0004-6361/201321554> (2013).
- [81] P. A. R. Ade, et al., DOI: <https://doi.org/10.1051/0004-6361/201525836> (2015).
- [82] K. Bamba, S. Nojiri, S. D. Odintsov & D. Sáez-Gómez, *Phys. Rev. D* **90**, 124061 (2014).
- [83] S. D. Odintsov & V. K. Oikonomou, *Annals of Physics* **363**, 503 (2015).
- [84] J. D. Barrow, *Physics Letters B* **235**, 40 (1990).
- [85] J. D. Barrow & A. R. Liddle, *Phys. Rev. D* **47**, 5219 (1993).
- [86] J. D. Barrow & N. J. Nunes, *Phys. Rev. D* **76**, 043501 (2007).